*Human Molecular Genetics*, 2020, Vol. 29, No. 18 3081–3093

**doi: 10.1093/hmg/ddaa199**
Advance Access Publication Date: 8 September 2020
General Article

GENERAL ARTICLE

# Aberrant early growth of individual trigeminal sensory and motor axons in a series of mouse genetic models of 22q11.2 deletion syndrome

Zahra Motahari[1,2], Thomas M. Maynard[3,†], Anastas Popratiloff[1,2], Sally A. Moody[1,2] and Anthony-S. LaMantia[3,4,*]

[1]Institute for Neuroscience, Washington, DC 20037, USA, [2]Department of Anatomy and Cell Biology, The George Washington University School of Medicine and Health Sciences, Washington, DC 20037, USA, [3]The Fralin Biomedical Research Institute at Virginia Tech-Carilion School of Medicine, Roanoke, VA 24016, USA and [4]Department of Biological Sciences, Virginia Tech, Blacksburg, VA 24060, USA

*To whom correspondence should be addressed. Email: anthonysl@vtc.vt.edu



## Abstract

We identified divergent modes of initial axon growth that prefigure disrupted differentiation of the trigeminal nerve (CN V), a cranial nerve essential for suckling, feeding and swallowing (S/F/S), a key innate behavior compromised in multiple genetic developmental disorders including DiGeorge/22q11.2 Deletion Syndrome (22q11.2 DS). We combined rapid *in vivo* labeling of single CN V axons in *LgDel*$^{+/-}$ mouse embryos, a genomically accurate 22q11.2DS model, and 3D imaging to identify and quantify phenotypes that could not be resolved using existing methods. We assessed these phenotypes in three 22q11.2-related genotypes to determine whether individual CN V motor and sensory axons wander, branch and sprout aberrantly in register with altered anterior–posterior hindbrain patterning and gross morphological disruption of CN V seen in *LgDel*$^{+/-}$. In the additional 22q11.2-related genotypes: *Tbx1*$^{+/-}$, *Ranbp1*$^{-/-}$, *Ranbp1*$^{+/-}$ and *LgDel*$^{+/-}$:*Raldh2*$^{+/-}$; axon phenotypes are seen when hindbrain patterning and CN V gross morphology is altered, but not when it is normal or restored toward WT. This disordered growth of CN V sensory and motor axons, whose appropriate targeting is critical for optimal S/F/S, may be an early, critical determinant of imprecise innervation leading to inefficient oropharyngeal function associated with 22q11.2 deletion from birth onward.

## Introduction

Many genetic disorders are thought to disrupt behavior by compromising early steps in neural circuit development (1,2). This early divergence may be subtle, variable and most likely impossible to define directly in humans. Indeed, resolving such partially penetrant cellular changes in early neural development has proven challenging in model organisms, including mice. First, defining behaviors, circuits and underlying developmental mechanisms in mutant mouse models that meaningfully parallel clinically significant deficits in human genetic disorders is difficult. Second, detecting changes in initial differentiation of individual neurons remain elusive—especially in early to mid-gestation embryos due to their small size and rapid rate of growth. We addressed these challenges by identifying early

†Thomas M. Maynard, http://orcid.org/0000-0001-6976-3936
**Received:** May 4, 2020. **Revised:** July 29, 2020. **Accepted:** September 1, 2020

divergence of axon growth in a key component—the trigeminal nerve of the developing neural circuit for a well-defined innate behavior, suckling, feeding and swallowing (3) in the genomically accurate *LgDel*$^{+/-}$ mouse model of DiGeorge/22q11.2 Deletion Syndrome (1,4), which in humans includes a high frequency of clinically significant disruptions of S/F/S from birth onward (3,5).

We showed previously that gross differentiation, gene expression and cellular composition in the trigeminal nerve (CN V) and ganglion (CNgV), which provides essential sensory innervation to regulate S/F/S, are disrupted in mid-gestation *LgDel*$^{+/-}$ embryos, prefiguring S/F/S difficulties at birth (6–8). Altered expression levels and patterns of several retinoic acid (RA) regulated genes in the hindbrain accompany these changes (6,8,9), including two genes within the 22q11.2 deletion: *Tbx1* and *Ranbp1*. *Tbx1*$^{+/-}$ embryos have cardiovascular and craniofacial dysmorphology; however, *LgDel*$^{+/-}$ hindbrain patterning and CN V phenotypes are absent even though there are posterior cranial nerve disruptions (6,10–12). *Ranbp1* is regulated by RA in WT embryos (9), and craniofacial development is disrupted in *Ranbp1* mutants (13). Finally, CN V phenotypes are absent when *LgDel*$^{+/-}$ RA-mediated hindbrain gene expression and patterning changes are returned toward WT due to diminished RA signaling that results from crossing *LgDel*$^{+/-}$ mice with those heterozygously deleted for *Raldh2*, the rate limiting RA synthetic enzyme (6,9,14). Using this series of 22q11.2-related genotypes, we assessed the relationship between changes in growth of individual CN V motor or sensory axons, altered hindbrain patterning and CN V differentiation.

CN V dysmorphology as well as altered RA-mediated gene expression is shared by two of these 22q11.2 genotypes: *LgDel*$^{+/-}$ and *Ranbp1*$^{-/-}$, but not the others. Accordingly, we asked whether disrupted RA-related patterning critically influences CN V axon growth in the context of 22q11.2 deletion. In addition, we recently reported statistically significant stochastic variation in gene expression levels across the entire *LgDel*$^{+/-}$ CNgV transcriptome (7). Thus, the penetrance of individual 22q11.2 gene-related CN V axon phenotypes, at least for sensory neurons, might vary substantially, perhaps due to cell-by-cell transcriptional variation. The small size of mid-gestation embryos and dynamism of cranial nerve morphogenesis raises challenges of adequate labeling and sufficiently large samples of individual axons to detect significant phenotypic change despite potential variability. We overcame these obstacles to identify disrupted individual CN V axon growth in register with CN V morphogenetic changes and altered RA-dependent hindbrain patterning in *LgDel*$^{+/-}$ and additional 22q11.2 mutants. This initial divergence may represent a first step of aberrant cranial nerve and hindbrain circuit development that results in disrupted S/F/S or other orofacial sensory-motor disruptions due to diminished 22q11.2 gene dosage.

## Results

### 22q11.2 gene mutations differentially disrupt CN V morphogenesis and axon fasciculation

We previously defined a partially penetrant gross CN V phenotype in *LgDel*$^{+/-}$ E10.5 embryos that is apparently related to an expansion of RA-dependent gene expression seen in the anterior hindbrain at E9.5 (6,8). To improve the resolution of these previous analyses, we used immunofluorescent anti-$\beta$III-tubulin labeling (3) as well as confocal microscopy in whole E10.5 embryos to better resolve the organization and trajectories of peripheral CN V axon fascicles. We note that the changes we summarize here for each genotype are also seen, albeit less clearly, in multiple additional samples of chromogenically labeled, conventionally imaged whole embryo preparations (3,6,8; Supplementary Material, Fig. S1). Many sensory and all motor neurons that constitute CN V in WT (Fig. 1A1–5) are derived from rhombomeres (r) 2–3, which do not express RA-regulated posterior identity genes (Fig. 1A2). The remaining CN V sensory neurons are derived from the trigeminal cranial placode (see Fig. 3N). CN V has three distinct distal branches, ophthalmic (op), maxillary (mx) and mandibular (md; Fig. 1A3). The proximal portions of the mx and md branches are distinguished by parallel axon fascicles (mx: arrows, Fig. 1A4; md: box, Fig. 1A5). Distal mx fascicles terminate in orderly sprays of smaller fascicles in the undifferentiated mesenchyme of branchial arch 1 A (Ba1A). Distal md fascicles divide into progressively smaller fascicles as this CN V branch extends ventrolaterally into Ba1B. As shown previously (3,6,8) in *LgDel*$^{+/-}$ embryos (Fig. 1B1) with a deletion of 28 contiguous 22q11.2 gene orthologues parallel to the minimal critical 22q11.2 deletion in humans (4), RA-regulated gene expression expands into r2–3 (Fig. 1B2, box). *LgDel*$^{+/-}$ CNgV retains its basic shape; however, all 3 CN V branches are less organized (Fig. 1B3). As shown previously (6,8), subsets of fascicles in mx (arrows, Fig. 1B4) and md branches (box, Fig. 1B3, and *insets*, Fig. 1B5) often appear misdirected and diminished in size. In the mx branch, these fascicles intersect, anastomose and terminate in a less ordered, comparatively sparse array of terminal extensions (arrowheads, Fig. 1B4) than the dense, ordered array of terminal fascicles of the WT mx branch. The distal superficial md branch (primarily CN V sensory axons, asterisk, Fig. 1B5) appears diminished, and the deep branch (primarily CN V motor axons, arrow, Fig. 1B5) is difficult to discern as a separate branch (compare arrows in Fig. 1A5 and B5). There appear to be fewer distal axon fascicles in the deep or superficial md branch and their terminal extensions are not as extensive as those in the WT md branch of CN V (arrows, arrowheads and asterisks, and *insets*, Fig. 1B5).

CN V gross differentiation, axon fasciculation, local trajectories and termination resembles either the WT or *LgDel*$^{+/-}$ pattern in 4 additional genotypes. In *Tbx1*$^{+/-}$ embryos (Fig. 1C1–5), previous studies have established that posterior branchial arches and cranial nerves are altered (6,10–12); however, hindbrain A–P patterning is unchanged and CN V is indistinguishable from WT (see also 6). In *Ranbp1*$^{-/-}$ mutants (Fig. 1D1), a 22q11.2 gene expressed in cranial neural crest whose loss of function disrupts branchial arch morphogenesis (13,15) and hindbrain patterning, replicates that in *LgDel*$^{+/-}$ (Fig. 1D2), as does CN V dysmorphology (Fig. 1D3). Based upon blind scoring (6,8) of each ganglion in a series of 10 *Ranbp1*$^{-/-}$, 20 *Ranbp1*$^{+/-}$ and 9 WT littermate embryos, we found that op, mx and md axon fascicles are shorter and appear less coherent than WT or *Ranbp1*$^{+/-}$ counterparts ($n = 12/20$ 60% *Ranbp1*$^{-/-}$, 13/40 = 32% *Ranbp1*$^{+/-}$ and 2/18 = 11% WT ganglia; $P = 0.002$, WT versus *Ranbp1*$^{-/-}$, $P = 0.1$, WT versus *Ranbp1*$^{+/-}$ (Supplementary Material, Fig. S1). Higher resolution confocal images of fluorescently labeled *Ranbp1*$^{-/-}$ CN V shows that the similar *Ranbp1*$^{-/-}$ and *LgDel*$^{+/-}$ gross CN V phenotypes are paralleled by comparable changes in fasciculation, anastomosis and termination of the mx (Fig. 1D4) and md (Fig. 1D5) branches. These changes in hindbrain patterning, CN V gross morphology, axon trajectory and fasciculation are not seen in *Ranbp1*$^{+/-}$ mutants (Fig. 1E1–5; Supplementary Material, Fig. S1). Finally, as shown previously (6), in *LgDel*$^{+/-}$ embryos carrying a single *Raldh2* null allele to reduce RA signaling (Fig. 1F; (14)), hindbrain patterning and CN V differentiation

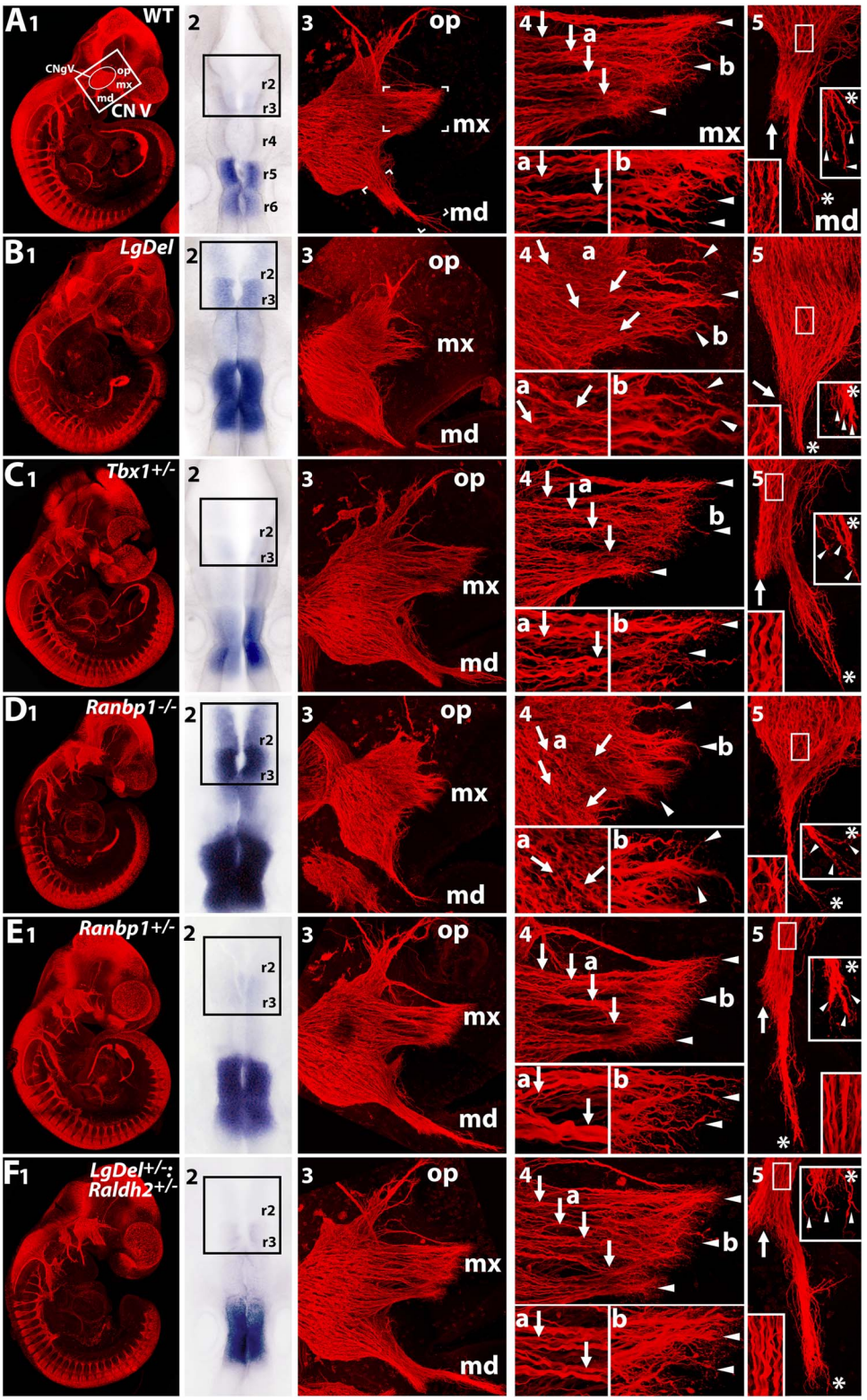


**Figure 1.** An overview of trigeminal nerve (CN V) dysmorphology and RA-dependent hindbrain patterning in a series of 22q11.2-related mutations. A total of 14 whole E10.5 embryos were imaged confocally. Eight: 1 WT, 4 *Tbx1*$^{+/-}$, 2 *Ranbp1*$^{+/-}$: and 1 *LgDel*$^{+/-}$:*Raldh2*$^{+/-}$ had CN V gross morphology that resembled that in WT identified previously in more extensive conventionally imaged samples (6–8; Supplementary Material, Fig. S1), and six: 3 *LgDel*$^{+/-}$ and 3 *Ranbp1*$^{-/-}$ had CN V gross morphology similar to that previously identified for *LgDel*$^{+/-}$ (6–8; Supplementary Material, Fig. S1). (**A1**) WT E10.5 embryo. CN V (box) and the trigeminal ganglion (CNgV; oval) are anterior in this lateral view. (**A2**) In the E9.5 WT hindbrain, *Cyp26b1*, detected by *in situ* hybridization, is seen in r5 and r6, but not r2, r3 or r4. (**A3**) A higher magnification confocal image of WT CNgV/CN V and its peripheral branches: ophthalmic (op), maxillary (mx) and mandibular (md); brackets indicate the regions of the mx and md branches shown in (4) and (5). (**A4**) The WT mx branch. Arrows (a) indicate parallel proximal axon fascicles; arrowheads (b) indicate limited terminal

resembles that in WT more than that *LgDel*$^{+/-}$. Accordingly, *Tbx1*$^{+/-}$, *Ranpb1*$^{-/-}$, *Ranbp1*$^{+/-}$ and *LgDel*$^{+/-}$:*Raldh2*$^{+/-}$ define a 22q11.2 mutant series in which several aspects of gross CN V differentiation, RA-dependent hindbrain patterning and CN V axon growth resemble either that in WT or *LgDel*$^{+/-}$ CN V.

## Rapid, quantifiable assessment of individual axon trajectories and targets

Previous analyses of cranial nerve axon growth, including extensive assessment of the CN V, have been carried out in dissected or histologically sectioned tissue after labeling the entire nerve. Many of these studies, done mostly at older embryonic stages, focused on the organization of sensory projections to the whisker pad via the mx branch of CN V (16,17). To assess divergent *LgDel*$^{+/-}$ and WT CN V sensory and motor axon growth phenotypes at earlier ages, prior to target differentiation, with single neuron/axon resolution, we needed a novel approach to sample randomly and characterize trajectories and targets of individual early embryonic CN V axons across each genotype that would: (i) result from targeted injections in live embryos with limited survival times; (ii) require minimal histological processing; (iii) label cells and axons in 3D; (iv) demonstrate the basic topographic organization of CN V sensory and motor neurons and axonal projections; (v) visualize individual axons from cell body to termini and (vi) permit reliable scoring and quantitative analysis.

We met these criteria using limited focal injections of fluorophore-conjugated biocytins in E11.5 living embryos at locations where relevant CN V axons are likely to project or CN V sensory neurons as well as motor axons are found (Fig. 2A). We pursued three injection strategies: one of three distinct fluorophore-conjugated biocytins was injected into the three primary target territories of CN V—ophthalmic (op), maxillary (mx) and mandibular (md)—to assess initial topography; these data are presented in Figure 3. Two different fluorophore-conjugated biocytins were injected into the mx and md region of CNgV to assess the initial projections of small numbers of axons as they extend toward mx or md targets; these data are presented in Figure 4. Finally, a single fluorophore-conjugated biocytin was injected into Ba1B only (md target) to retrogradely label subsets of individual CN V sensory and motor axons (CN V motor neurons innervate only md targets) as well as their cell bodies of origin; these data are presented and analyzed statistically in Figures 5 and 6. After a 1.5 h survival *ex vivo*, fixation and minimal histological processing (Fig. 2B), cell bodies of origin were identified, labeled axon fascicles resolved, and individual CN V axons that extend considerable distances to central and peripheral targets reconstructed through 3D confocal image stacks (Fig. 2B). Each labeled axon was recorded as a 3D dataset. We used unbiased computational methods to reliably trace individual labeled axons from peripheral or central terminations to their parent cell bodies. Thus, we defined a novel approach that visualizes CN V axon growth with sufficient resolution to permit the analysis of CN V topography, projections and individual axon trajectories.

## Identity and distribution of early CN V projection neurons in WT and *LgDel*$^{+/-}$

We first asked whether nascent CN V sensory or motor neuron identities and positions in CNgV or the anterior hindbrain, respectively, are comparable in *LgDel*$^{+/-}$ versus WT embryos at E11.5. By E11.5 CNgV has coalesced into a coherent ganglion (6,18), much of hindbrain motor neurogenesis is complete (19), and the three major CN V branches are distinct. We made limited injections of three spectral variants of biocytin into the peri-ocular (op; blue), maxillary (mx, red) and mandibular (md, green) mesenchyme of living *ex vivo* WT and *LgDel*$^{+/-}$ embryos and assessed the locations of retrogradely labeled cells in CNgV (Fig. 3). CN V sensory neurons can be labeled selectively from the territories all three CN V branches in *LgDel*$^{+/-}$ and WT embryos (Fig. 3A–F, H–L). Within CNgV, sensory neurons segregate in an A–P manner corresponding, respectively, to peri-ocular (op), Ba1A (mx) and Ba1B (md) targets. We detected no gross differences in the distribution of retrogradely labeled cells in WT versus *LgDel*$^{+/-}$ E11.5 CNgV ($n = 6$ WT, $n = 8$ *LgDel*$^{+/-}$ embryos). Similarly, retrogradely labeled motor neurons—only from Ba1B (md) injection, as expected—in *LgDel*$^{+/-}$ and WT embryos do not differ in their position or distribution in the region of the anterior hindbrain where the trigeminal motor nucleus will form (Fig. 3G and M). Finally, we assessed cranial placode versus neural crest derivation of early projecting CN V neurons. Most, if not all, CN V sensory neurons that project into Ba1B at E11.5 express the transcription factor Six1 (18,20,21) and are therefore likely derived from the trigeminal cranial placode (Fig. 3N–P). Thus, based upon similar segregation of CN V sensory neurons projecting to op, mx and md territories, and similar hindbrain position of md projecting CN V motor neurons, it appears that initial positions of CN V sensory and motor neurons do not differ substantially in *LgDel*$^{+/-}$ and WT E11.5 embryos.

## Precision of sensory and motor axon Growth in WT and *LgDel*$^{+/-}$ embryos

We next asked whether smaller subsets of individual axons fasciculate and extend from CNgV or hindbrain motor neurons with equivalent fidelity to Ba1A (mx) or Ba1B (md) targets. We made injections of two distinct fluorophore conjugated biocytins into the mid-anterior or posterior portion of E11.5 CNgV (Fig. 4), to visualize axons projecting into either Ba1A (mx) or Ba1B (md). Axons labeled by this approach fasciculate tightly as they extend into Ba1A (anterior) or Ba1B (posterior) in WT ($n = 10$) and *LgDel*$^{+/-}$ embryos ($n = 13$; Fig. 4A and C). Once sensory axons enter the hindbrain, they issue anterior branches toward the presumptive principle trigeminal sensory

defasciculation. (a) digitally enlarged images of region indicated by arrows showing segregated parallel fascicles, and (b) the region indicated by the arrowheads showing WT axon terminations. (**A5**) Axons of a deep branch of the md division of CN V (arrow) enter Ba1B mesenchyme. A superficial branch terminates in an array of smaller fascicles (asterisk). Upper *inset*: terminal defasciculation of the superficial branch. Lower *inset*: fasciculation in the proximal md branch. (**B1**) An E10.5 *LgDel*$^{+/-}$ embryo. (**B2**) *LgDel*$^{+/-}$ *Cyp26b1 in situ* hybridization at E9.5 (**B3**) CNgV and peripheral branches of CN V. (**B4**) Digitally enlarged views of mx (4) and md (5) branches. Arrows in (4) indicate smaller fascicles that appear less uniform than WT parallel arrays (A4, a). Arrowheads indicate *LgDel*$^{+/-}$ terminal fascicles, which appear less dense and organized than WT (A4, b). (**B5**) The md branch is diminished, terminal defasciculation is impoverished (asterisk, upper *inset*) and proximal fascicles are disordered (lower *inset*). (**C1–5**) *Tbx1*$^{+/-}$ E10.5 CN V, E9.5 hindbrain patterning, mx and md axon organization does not differ noticeably from WT. (**D1**) *Ranbp1*$^{-/-}$ E10.5 embryo. (**D2**) E9.5 *Ranbp1*$^{-/-}$ hindbrain patterning. (**D3**) *Ranbp1*$^{-/-}$ CNgV and CN V branches. (**D4**) *Ranbp1*$^{-/-}$ mx fasciculation and termination appears similar or potentially more severe than that in *LgDel*$^{+/-}$ (A4, a, b). (**D5**) *Ranbp1*$^{-/-}$ md fasciculation and termination appears similarly compromised as that in *LgDel*$^{+/-}$. (**E1–5**; **F1–5**) *Ranbp1*$^{+/-}$ and *LgDel*$^{+/-}$:*Raldh2*$^{+/-}$ E10.5 CN V, E9.5 hindbrain patterning, mx and md axon organization does not differ noticeably from WT.

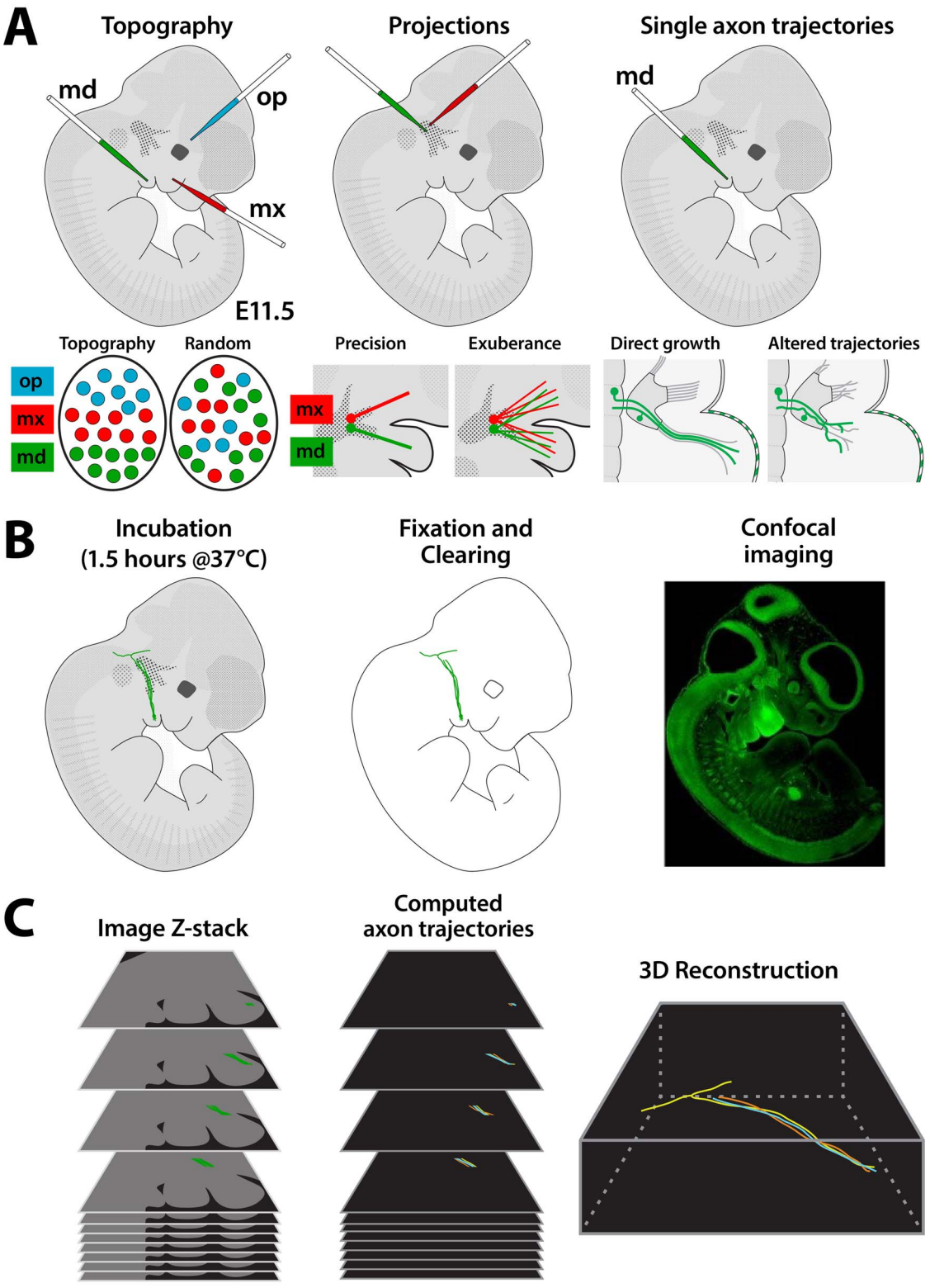


**Figure 2.** Key aspects of initial CN V differentiation can be resolved with a new rapid *ex vivo* direct fluorophore-conjugated biocytin injection/tracing method combined with high-resolution laser confocal microscopic imaging in mid-gestation mouse embryos. (**A**) Injection strategies to resolve initial topographic segregation (*left*), precise versus exuberant axon growth (*middle*) and single axon trajectories (*right*) in E11.5 embryos. (**B**) Summary of post-injection incubation/survival (1.5 h at 37° in Leibovitz L-15 medium; *left*) with histological processing limited to whole embryo clearing after fixation (*middle*) prior to confocal imaging of the whole embryo (*right*). A complete sagittal optical section from a 3D image set of a whole embryo that received a single fluorochrome-conjugated biocytin injection into distal Ba1B (md) is shown. (**C**) Z-stacks of images of single labeled axons can be analyzed to assess the trajectory and branching of the axon in 3D (*left*). These images are then further digitally analyzed to track individual axons through the optical sections of the Z-stack (*middle*) and then display each axon in 3D space to assess CN V organization with single axon resolution (*right*).

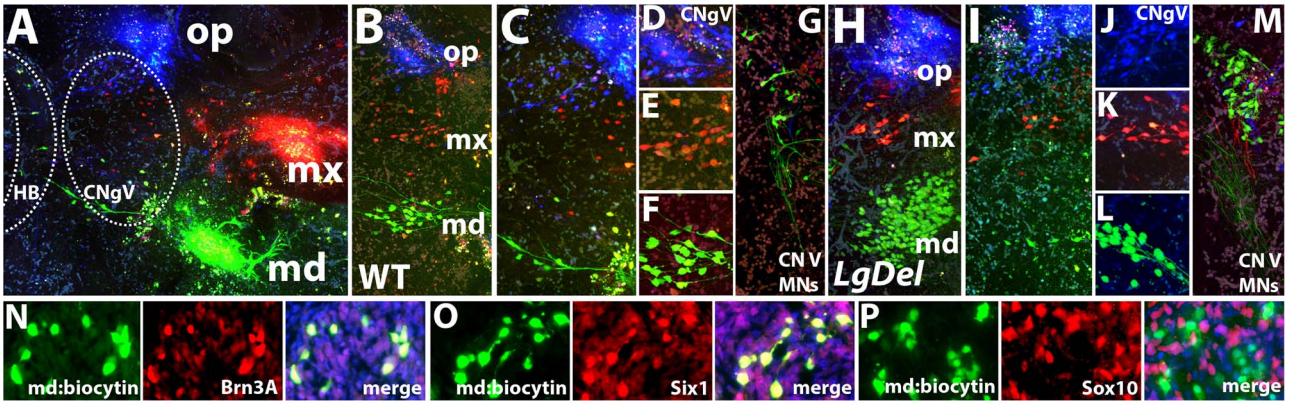


**Figure 3.** The initial segregation of sensory and motor cells of origin into ophthalmic, maxillary and mandibular projecting populations is not substantially disrupted by 22q11.2 gene deletion during the initial differentiation of CN V. (**A**) Broad field image of injections of 3 distinct fluorophore-conjugated biocytins into the target territories of the op (blue), mx (red) and md (green) branches of CN V in a WT E11.5 embryo. The region of CNgV is indicated by a dotted circle, and the adjacent hindbrain (HB), the site of md-projecting CN V motor neurons, is outlined by dotted lines. (**B, C**) Two examples of WT CNgV showing segregation of op (blue), mx (red) and md (green) projecting CN V sensory neurons. (**D–F**) Digitally enlarged images of individual retrogradely labeled CN V sensory neurons that project to op, mx and md territories. (**G**) Localized labeling of CN V motor neurons projecting via the md branch, in the WT hindbrain. (**H, I**) Retrogradely labeled op (blue), mx (red) and md (green) CN V sensory neurons are segregated in *LgDel*$^{+/-}$ E11.5 embryos, similar to that in WT, following biocytin injection into respective target territories. (**J–L**) Digitally enlarged images of individual retrogradely labeled op (blue), mx (red) and md (green) *LgDel*$^{+/-}$ CN V sensory neurons. (**M**) Similar location and segregation of md-projecting CN V motor neurons in the hindbrain adjacent to CNgV in *LgDel*$^{+/-}$ embryos. (**N–P**) Combined retrograde labeling of CN V sensory neurons following Ba1B (md) injection (green, *left*) with immunohistochemical labeling for markers associated with differentiating sensory neurons that extend axons (Brn3A, red, *middle*, N); cranial placode derived CN V sensory neurons (Six1, red, *middle*, O) or rhombomere 2/3 neural crest derived sensory neurons/precursors (Sox10, red, *middle*, P). The retrogradely labeled CN V neurons express Brn3A and Six1 (yellow label, *right*, N, O), but not Sox10 (almost no registration between red and green label, *right*, P).

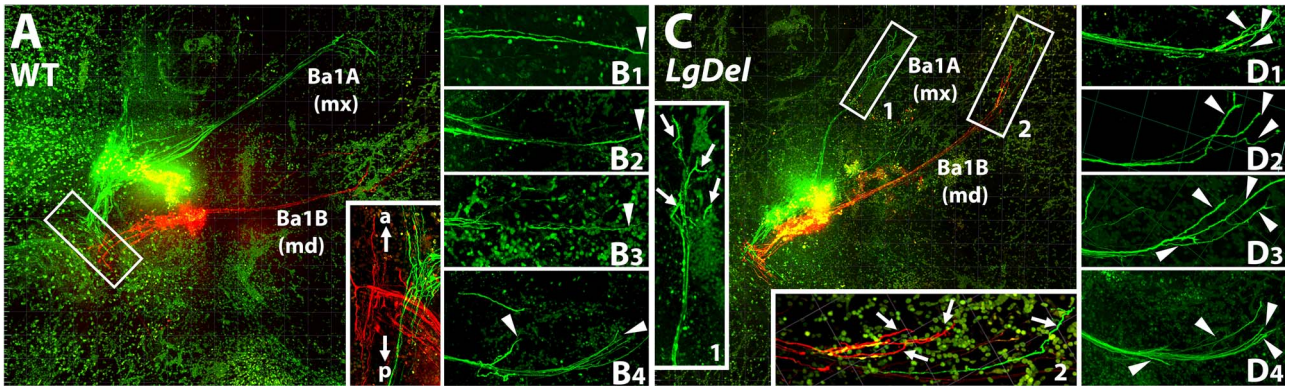


**Figure 4.** Projections of CN V sensory and hindbrain motor neurons into presumptive mx and md targets are precise in WT and *LgDel*$^{+/-}$ embryos; however, there is an apparent increase in terminal branching and defasciculation in *LgDel*$^{+/-}$. (**A**) Focal injections of two distinct fluorophore-conjugated biocytins into the presumed mx (green) and md (red) portions of E11.5 WT CNgV label single axon fascicles that project linearly and precisely into Ba1A (mx; green) and Ba1B (md; red). In addition, the proximal (hindbrain) projections from these sensory neurons (*inset*) bifurcate, with one branch directed anteriorly (a, arrow), and the other posteriorly (p, arrow). The Ba1A hindbrain sensory axon branches (green) are more medial, and the Ba1B branches are more lateral. (**B1–3**) The terminations of individual distal fascicles tend to be coherent and unbranched; however, some examples of terminal branching (**B4**) are seen in WT. (**C**) Focal injection of two distinct fluorophore-conjugated biocytins into presumed mx (green) and md (red) portions of E11.5 *LgDel*$^{+/-}$ CNgV labels axon fascicles that project to their respective targets, Ba1A and Ba1B. There is, however, terminal defasciculation (box 1, arrows, *inset*). In addition, in both *LgDel*$^{+/-}$ and WT, we see aberrant fascicles seen in inappropriate territories (box 2, arrows, *inset*) at fairly low, but equivalent penetrance in both genotypes. (**D1–4**) The termini of labeled axon fascicles are more branched (arrowheads) and extend in multiple directions than those in WT.

nucleus, and posterior branches toward the presumptive spinal trigeminal nucleus. These Ba1A(mx) and Ba1B (md) central projections remain segregated (Fig. 4A, box and inset). There are occasional single axons labeled by anterior or posterior injection that project to the opposite target territory in WT (4/10 = 40%) and *LgDel*$^{+/-}$ (5/13 = 38%; Fig. 4C, insets). There was, however, one potential distinction between WT and *LgDel*$^{+/-}$. In all WT embryos analyzed, CN V axons extend directly toward mx and md targets, with limited branching near their terminations (Fig. 4B1–4; 10/10 embryos). In contrast, in a small subset of *LgDel*$^{+/-}$ embryos, individual axons apparently branch before reaching peripheral targets (3/13 = 23%, Fig. 4C, insets). In addition, in *LgDel*$^{+/-}$, at their terminations in Ba1A and Ba1B, small axon fascicles or individual axons are arrayed more broadly in more diverse directions (Fig. 4D1–4; 4/13 or 31% *LgDel*$^{+/-}$ versus 1/10 or 10% WT embryos). Thus, WT CN V sensory and motor axons extend selectively into Ba1A or Ba1B and fasciculate according to CNgV or anterior hindbrain position. *LgDel*$^{+/-}$ CN V axon growth, however, may be less consistent, mirroring diminished coherence that defines the partially penetrant *LgDel*$^{+/-}$ gross CN V phenotype.

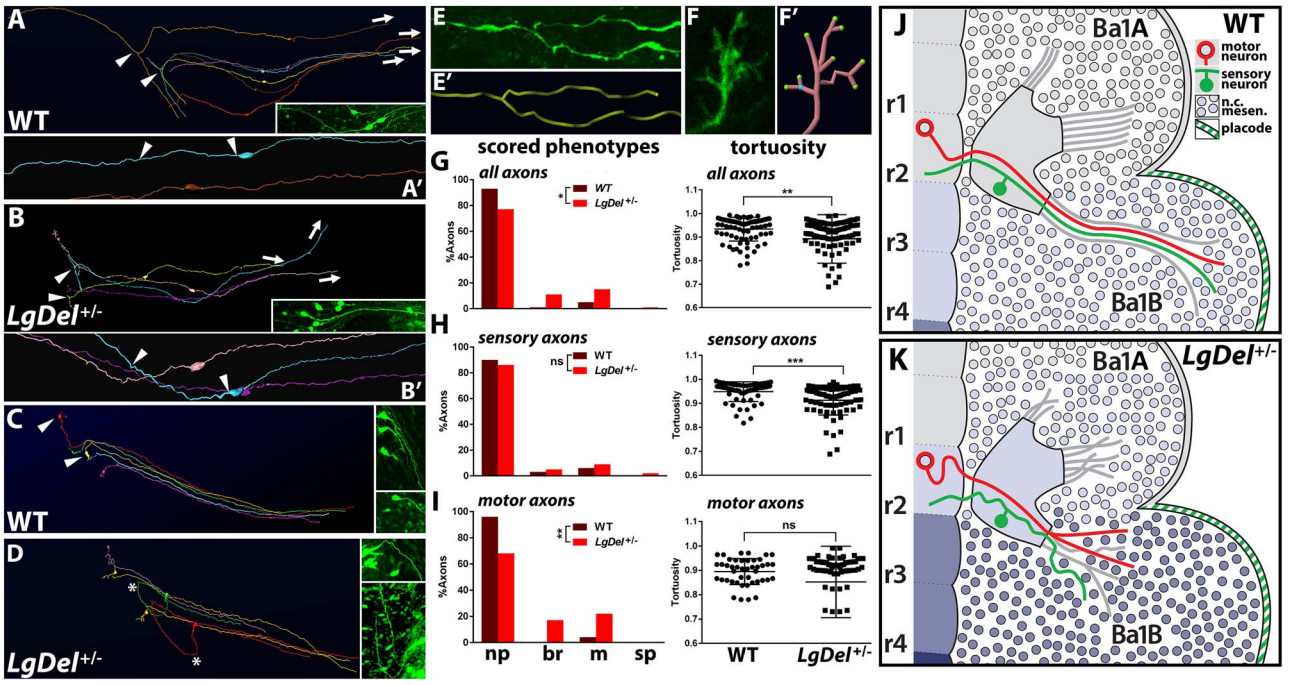


**Figure 5.** Diminished 22q11.2 gene dosage in *LgDel*$^{+/-}$ embryos destabilizes CN V sensory and motor axon growth. (**A**) 2D renderings of 3D reconstructions of WT proximal (left) and distal (right) segments of CN V md sensory axons labeled after distal Ba1B injection identified by direct continuity with CNgV cell bodies of origin. Arrows: similar directions of growth for WT distal and proximal axons. Arrowheads: bifurcation of CN V sensory axon proximal/central branches. *Inset*: 2D renderings of a confocal image stack of CN V sensory neurons and their distal/proximal axons. (**A′**) 2D rendering of two WT CN V md sensory neurons showing relatively linear extension of distal and proximal axons (e.g. axon segment indicated between the two arrowheads) (**B**) 2D renderings of *LgDel*$^{+/-}$ CN V md sensory axons and CNgV parent cell bodies; distal and proximal *LgDel*$^{+/-}$ segments have more diverse directions of growth (arrows) than WT counterparts. *Inset*: 2D image of a CN V sensory axon and parent cell body. (**B′**) Apparently increased tortuosity (e.g. axon segment between arrowheads) of *LgDel*$^{+/-}$ CN V distal and proximal sensory axons. (**C**) 2D renderings of WT CN V motor axons from motor neurons. After an ~90° turn upon exiting the hindbrain (arrowheads), the axons extend directly toward Ba1B. *Insets*: Representative images of WT CN V motor neurons. (**D**) 2D renderings of *LgDel* CN V motor axons. Some CN V motor neuron axons (asterisks) diverge substantially from the WT pattern of hindbrain exit and direct extension toward Ba1B. *Inset*: Representative images of *LgDel*$^{+/-}$ motor neurons with varying degrees of axon misrouting. (**E**, **E′**) Digital enlargement and Imaris-generated reconstruction showing local branching of a *LgDel*$^{+/-}$ CN V axon. (**F**, **F′**) Digital enlargement and Imaris-generated reconstruction showing terminal sprouting of a *LgDel*$^{+/-}$ CN V axon. (**G**) Quantitative summaries of phenotypic frequencies (branching: br; misrouting: m; sprouting: sp; *left*,$^{*}P = 0.02$, no phenotype: np;) and tortuosity (*right*, $^{**}P = 0.003$) for all individual WT ($n = 56$ axons) and *LgDel*$^{+/-}$ ($n = 84$ axons/18 embryos) CN V axons (sensory and motor). (**H**) Phenotypic frequencies (*left*) and tortuosity (*right*) for WT ($n = 30$ axons) and *LgDel*$^{+/-}$ ($n = 43$ axons) CN V sensory axons. (**I**) Phenotypic frequencies (*left*) and tortuosity (*right*) for WT ($n = 26$ axons) and *LgDel*$^{+/-}$ ($n = 41$ axons) CN V motor axons. (**J**, **K**) Schematic of major features of early WT and *LgDel*$^{+/-}$ CN V sensory and motor axon growth.

## Divergent growth of individual WT versus *LgDel*$^{+/-}$ CN V sensory and motor axons

The apparent disorganization of CN V axon fascicles in *LgDel*$^{+/-}$ embryos suggests that disordered growth of subsets of individual sensory or motor axons may contribute to divergent CN V differentiation due to diminished 22q11.2 gene dosage. Nevertheless, limited labeling of multiple axon in single fascicles cannot securely resolve these differences. Accordingly, we adapted our *ex vivo* injection strategy to label substantial portions of individual distal (peripheral) and proximal (central) CN V sensory and motor axons using small biocytin injections into distal Ba1B (Table 1 and Fig. 5). These labeled axons can be imaged and traced digitally in 3D to their sensory or motor neuron sources as well as apparent terminations (Fig. 5A–D) using unbiased computational axon tracking. This approach, which randomly labels very few axons in each embryo, does not address gross CN V phenotypes in each embryo and thus has not been analyzed statistically on a per embryo basis (see Table 1). Nevertheless, the proportions of embryos of each genotype with at least one 'phenotypic' axon (see below) are in register with the frequency of gross CN V phenotypes identified based upon whole embryo labeling in the same genotypes (Table 1; Supplementary Material, Fig. S1; (6)).

In an initial assessment of axon growth and trajectory in a limited sample of individually labeled WT and *LgDel*$^{+/-}$ axons, blind to genotype, we noticed variations in individual axon differentiation that we categorized as potential phenotypes (Fig. 5A–F). There was a noticeable subset of bifurcated or more extensively branched distal axons among more common unbranched axons that grow directly into the periphery. In addition, there were misrouted axons growing in directions inconsistent with known targets. We also identified one axon in which multiple small branches emerged at the axon terminus. Based upon this initial survey, these variations were defined as phenotypic categories for blind scoring of a larger sample of WT and *LgDel*$^{+/-}$ axons. Finally, we noticed local undulations in some axons, rather than the straight extension seen in others. To determine whether these apparent aberrations within the initial sample of individual *LgDel*$^{+/-}$ versus WT axons represent statistically distinct CN V axon phenotypes, we compared the frequency of each across a larger sample of axons for each genotype (Table 1). We imaged and reconstructed in 3D from apparent terminations to cell bodies of origin 314 individual axons from 62 embryos of 6 different genotypes (including WT), all blind to genotype, to complete this analysis (Table 1).

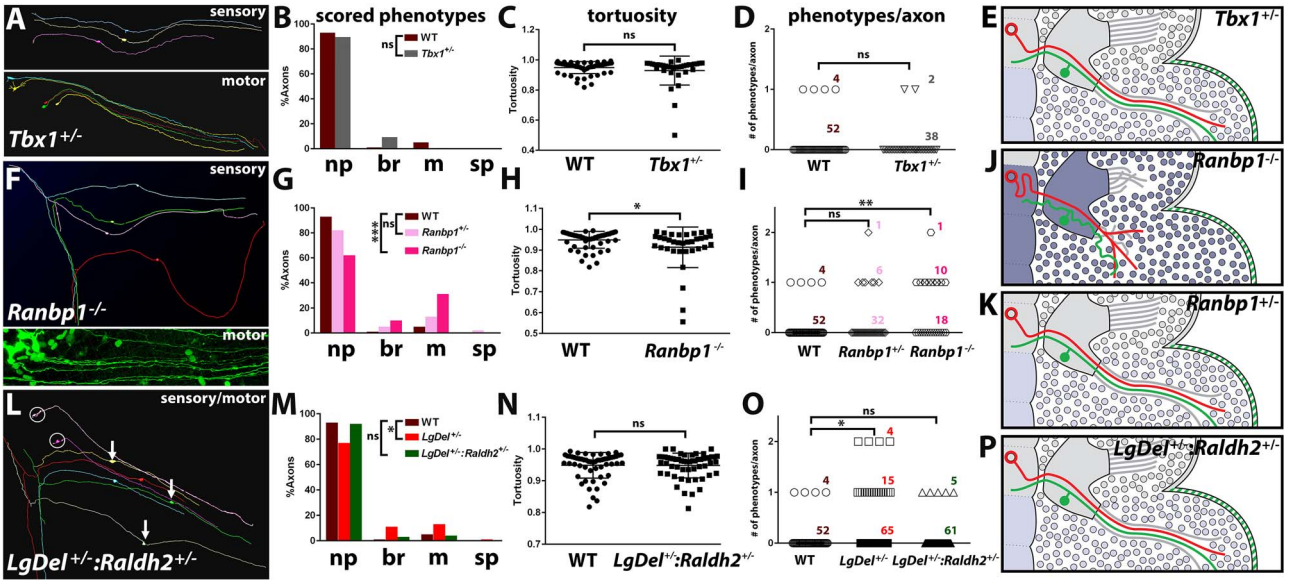


**Figure 6.** Frequency of destabilized individual axon growth varies in register with changes in RA-mediated patterning in a series of 22q11.2 gene-related mutant axons. (**A**) 2D renderings of individual CN V sensory neurons and their distal and proximal axons (*top*), and CN V motor neurons and their distal axons (*bottom*) from *Tbx1*$^{+/-}$ mutant. (**B**) Frequency of branching, misrouting and sprouting CN V axon phenotypes in *Tbx1*$^{+/-}$ compared with WT. (**C**) CN V axon tortuosity in *Tbx1*$^{+/-}$. (**D**) Comparison of number of phenotypes/axon in *Tbx1*$^{+/-}$ versus WT embryos. Numbers of axons analyzed in each category are given to the right of the graphic record. (**E**) Individual CN axon growth in *Tbx1*$^{+/-}$ embryos resembles that in WT, as does hindbrain A–P patterning. (**F**) 2D renderings of *Ranbp1*$^{-/-}$ CN V sensory neurons and their proximal and distal axons (top) and confocal image of *Ranbp1*$^{-/-}$ CN V motor neurons and their distal axons (bottom). (**G**) Frequency of branching, misrouting and sprouting CN V axon phenotypes in *Ranbp1*$^{-/-}$ and *Ranbp1*$^{+/-}$ compared with WT controls. (**H**) CN V axon tortuosity in *Ranbp1*$^{-/-}$ compared with WT. (**I**) Comparison of number of phenotypes/axon in *Ranbp1*$^{-/-}$, *Ranbp1*$^{+/-}$ and WT. (**J**) Growth and trajectories of individual *Ranbp1*$^{-/-}$ axons are similar, but apparently more frequent and severe than those in *LgDel*$^{+/-}$, in register with similar but more substantial changes in A–P hindbrain patterning. (**K**) Growth and trajectory of individual *Ranbp1*$^{+/-}$ axons is similar to WT, as is hindbrain A–P patterning. (**L**) 2D renderings of CN V motor neurons (circles) and sensory neurons (arrows) in *LgDel*$^{+/-}$:*Raldh2*$^{+/-}$. (**M**) Frequency of branching, misrouting and sprouting in *LgDel*$^{+/-}$:*Raldh2*$^{+/-}$ versus WT CN V axons. (**N**) CN V axon tortuosity in *LgDel*$^{+/-}$:*Raldh2*$^{+/-}$. (**O**) Comparison of number of phenotypes/axon in *LgDel*$^{+/-}$:*Raldh2*$^{+/-}$ versus WT. (**P**) Growth and trajectory of individual *LgDel*$^{+/-}$: *Raldh2*$^{+/-}$ axons is similar to WT, in parallel with the rescue of hindbrain A–P patterning toward WT.

**Table 1.** Summary of genotypes, litters embryos, percentages of embryos with at least one phenotypic axon (% pheno.), the ranks of phenotypic frequency, total numbers of axons, % axons with at least one phenotype (% pheno. axons), and ranks

| Genotype | Litters | Embryos (ganglia) | % Pheno. | Rank | *n* axons | % Pheno. axons | Rank | % Gross pheno | Rank |
|---|---|---|---|---|---|---|---|---|---|
| WT | 9 | 13 | 30% (4/13) | 5 | 56 | 7% (4/56) | 5 | 17%* | 5 |
| *LgDel*$^{+/-}$ | 10 | 18 | 55% (10/18) | 2 | 84 | 23% (19/84) | 2 | 42%* | 2 |
| *Tbx1*$^{+/-}$ | 5 | 8 | 25% (2/8) | 6 | 40 | 5% (2/40) | 6 | 27%* | 4 |
| *Ranpb1*$^{+/-}$ | 4 | 6 | 50% (3/6) | 3 | 39 | 18% (7/39) | 3 | 32% | 3 |
| *Ranbp1*$^{-/-}$ | 4 | 6 | 80% (4/6) | 1 | 29 | 38% (11/29) | 1 | 60% | 1 |
| *LgDel* $^{+/-}$:*Raldh2*$^{+/-}$ | 6 | 11 | 36% (4/11) | 4 | 66 | 8% (5/66) | 4 | 0%* | 6 |

In addition, in the two columns at far right, the frequency of CN V gross phenotypes (% gross pheno.) and ranks for based upon data from previous studies (*Karpinski *et al.* 6) or the present study (*Ranbp1*$^{+/-}$; *Ranbp1*$^{-/-}$)

Individual WT sensory (Fig. 5A) and motor axons (Fig. 5C) extended toward the periphery in a fairly consistent direction. In contrast, there was more departure from direct peripheral extension for individual *LgDel*$^{+/-}$ sensory (Fig. 5B) and motor axons (Fig. 5D). To determine whether the frequency or degree of the four potential phenotypes: branching (Fig. 5E and E′), misrouting (see Fig. 5D, asterisks), sprouting (Fig. 5F and F′) and degree of tortuosity (see Fig. 5B′, arrowheads) differs in the two genotypes, we scored or measured these divergent features of axon growth in a total of 142 individual axons (56 WT, 86 *LgDel*$^{+/-}$) labeled and reconstructed from 31 embryos (13 WT, 18 *LgDel*$^{+/-}$) collected from 19 litters (9 WT, 10 *LgDel*$^{+/-}$; Table 1). In the entire sample of axons in each genotype, we found that the three scored phenotypes, based upon descriptive characteristics of axon variation, were significantly more frequent in *LgDel*$^{+/-}$ than WT embryos (Fig. 5G; $n = 56$ axons WT, 84 axons *LgDel*$^{+/-}$; $P = 0.02$; Fisher Exact/Chi Square). Tortuosity, measured as the ratio of the distance of a straight line from the point of axon initiation at the parent cell body to its distal termination in the periphery divided by the actual length of the axon, was significantly lower in *LgDel*$^{+/-}$, which indicates increased tortuosity ($P = 0.003$, *t*-test). Altogether, these data demonstrate that there is increased variation in distinct aspects of individual *LgDel*$^{+/-}$ versus WT CN V axon growth based upon the four potential phenotypes we identified prior to comparing the two genotypes.

We next asked whether this apparent phenotypic variation was distinct for CN V sensory versus motor axons. It seemed possible that there might be differences based upon the distinct placodal (sensory) versus neural tube neuroepithelium (motor) origins of the two populations at this stage of differentiation (see

Fig. 3N–P). The scored phenotypes, branching and misrouting, were slightly elevated in *LgDel*$^{+/-}$ CN V sensory ($n = 43$) versus WT sensory ($n = 30$) axons; however, this increase did not reach statistical significance ($P = 0.88$; Fisher Exact/Chi Square; Fig. 5H, *left*). Nevertheless, *LgDel*$^{+/-}$ sensory axons were significantly more tortuous than their WT counterparts ($P = 0009$; *t*-test; Fig. 5H, *right*). In contrast, scored phenotypes were significantly more frequent in *LgDel*$^{+/-}$ motor ($n = 41$) versus WT motor ($n = 26$) axons ($P = 0.0083$; Fig. 5I, *left*), whereas tortuosity, though somewhat elevated in *LgDel*$^{+/-}$ motor axons, did not differ significantly for between the two genotypes ($P = 0.08$; Fig. 5I, *right*). Apparently, there is an increase in the frequency of several phenotypes, defined a priori, in *LgDel*$^{+/-}$ versus WT CN V axons (Fig. 5J and K). The frequency of these phenotypes increases for sensory and motor axons in *LgDel*$^{+/-}$; however, the scored phenotypes are statistically distinct only for motor axons, whereas tortuosity is statistically distinct only for sensory axons. Thus, as sensory and motor axons intermingle and grow to their peripheral Ba1B targets, they growth as a group is significantly more likely disordered and misdirected.

### Divergent individual CN V axon growth in a series of 22q11.2-related mutants

These changes in axon growth may contribute to altered CN V differentiation that accompanies altered hindbrain patterning due to 22q11.2 deletion. If this is the case, they should be seen at lower frequency or absent in 22q11.2-related genotypes in which patterning and CN V gross phenotypes parallel WT (see Fig. 1 and Table 1), and at higher frequency in those in which the *LgDel*$^{+/-}$ hindbrain patterning change is recapitulated or enhanced. To assess whether the single axon phenotypes might contribute to anomalous CN V gross differentiation, we analyzed CN sensory and motor axons in four 22q11.2-related genotypes without or with hindbrain patterning changes and accompanying CN V dysmorphology (see Fig. 1): *Tbx1*$^{+/-}$, *Ranbp1*$^{-/-}$, *Ranbp1*$^{+/-}$ and *LgDel*$^{+/-}$:*Raldh2*$^{+/-}$ compound mutants.

Heterozygous *Tbx1* deletion does not alter A–P hindbrain patterning or CN V gross morphology [see Fig. 1C; (6)]. In parallel, we found no evidence of significantly altered individual CN V axon growth across the *Tbx1*$^{+/-}$ genotype (Fig. 6A), based upon either the scored phenotypes or tortuosity ($n = 40$ axons; 22 sensory axons, 18 motor axons; Fig. 6B and C). The number of phenotypes/axon in *Tbx1*$^{+/-}$ is not significantly different from WT ($P > 0.99$; one-way ANOVA with Bonferroni correction, Fig. 6D). Thus, in the absence of an RA-mediated A–P patterning shift or gross CN V dysmorphology, but in the context of heterozygous deletion of *Tbx1*, a single 22q11.2 gene associated with additional 22q11 deletion-related pharyngeal and cardiovascular phenotypes, individual CN V growth is not compromised as it is in individual *LgDel*$^{+/-}$ CN V axons (Fig. 6E).

In the *Ranbp1*$^{-/-}$, disrupted craniofacial and CN V differentiation is similar or perhaps even more severe than in *LgDel*$^{+/-}$ (13; see Fig. 1 and Supplementary Material, Fig. S1), and individual sensory and motor axon trajectories also appear compromised (Fig. 6F). The scored phenotypes that are more frequent among individual *LgDel*$^{+/-}$ axons are also more frequent for individual *Ranpb1*$^{-/-}$ axons (29 axons; 14 sensory, 15 motor; $P = 0.0009$; Fisher Exact/Chi Square, Fig. 6G) and these axons are also more tortuous ($P = 0.05$, Fig. 6H). The number of phenotypes/axon in *Ranbp1*$^{-/-}$ is significantly higher than WT ($P = 0.0017$; one-way ANOVA with Bonferroni correction, Fig. 6I). In contrast, *Ranbp1*$^{+/-}$ axon growth or targeting, based on our scored or measured phenotypes, is neither significantly different from WT (Fig. 6G and H; $n = 39$ axons; 20 sensory, 19 motor) nor do numbers of phenotypes/axon differ significantly (Fig. 6I). Thus, disrupted growth of individual CN V axons is enhanced in *Ranbp1*$^{-/-}$ where hindbrain patterning changes and CN V dysmorphology parallel or surpass those in *LgDel*$^{+/-}$ (Fig. 6J). The lack of phenotypic change in *Ranbp1*$^{+/-}$ CN V axons (Fig. 6K) indicates that *Ranbp1* heterozygous deletion alone cannot explain CN V dysmorphology due to full 22q11.2 gene deletion.

We finally asked whether a genetic rescue of the RA-dependent A–P hindbrain patterning (see Fig. 1; 6), accomplished by crossing *LgDel*$^{+/-}$ with *Raldh2*$^{+/-}$, which lowers RA signaling by at least 35% (9) also modifies trajectories and targeting of individual CN V sensory and motor axons toward WT frequencies (Fig. 6L). In these *LgDel*$^{+/-}$:*Raldh2*$^{+/-}$ embryos, the frequency of CN V axon phenotypes is indistinguishable from WT ($n = 66$ axons; 35 sensory, 31 motor; $P = 0.89$; Fig. 6M), as is tortuosity ($P = 0.47$; Fig. 6N). The number of phenotypes/axons for *LgDel*$^{+/-}$:*Raldh2*$^{+/-}$ axons also approximates WT ($P > 0.99$) and is significantly less than in *LgDel*$^{+/-}$ ($P = 0.03$; Fig. 6O). Thus, the growth and trajectories of individual *LgDel*$^{+/-}$:*Raldh2*$^{+/-}$ axons is similar to that in WT (Fig. 6P). Apparently, disrupted RA-dependent A–P hindbrain patterning in *LgDel*$^{+/-}$ is a key determinant of the capacity of individual CN V sensory and motor axons to grow efficiently and directly to their targets.

## Discussion

We have shown that disordered growth of individual trigeminal (CN V) sensory and motor axons increases in correlation with disrupted RA-mediated A–P hindbrain patterning and gross disruption of CN V differentiation caused by heterozygous deletion of multiple 22q11.2 genes or full loss of function or single 22q11.2 gene *Ranbp1*. These partially penetrant axon anomalies do not prevent the initial segregation of CN V into three recognizable branches that will innervate op, mx and md targets. Instead, these changes in axon growth may contribute to local defasciculation and disorganization within each CN V branch, especially the mx and md branches. Of the six genotypes analyzed here, these axon anomalies are only detected in the two genotypes in which A–P hindbrain patterning is altered, so RA-dependent gene expression expands into anterior rhombomeres that give rise to subsets of CN V sensory and all CN V motor neurons. Apparently, sequential disruption of the earliest steps of patterning, in part mediated by *Ranbp1* as well as altered RA signaling in the hindbrain, significantly increases the frequency of aberrant growth for subsets of individual CN V axons. This increased probability of altered axon growth is in register with increased probability of disrupted initial differentiation of CN V and may contribute to oropharyngeal dysfunction in newborn *LgDel*$^{+/-}$ mice (5,6), including suckling, feeding and swallowing difficulties that resemble those in infants and toddlers with 22q11DS.

### Analyzing CN V axon growth in mid-gestation mouse embryos

Previous studies of early CN V axon growth have focused on the organization of ophthalmic projections to the cornea or maxillary projections to the developing whisker pad at later stages of fetal development or early post-natal life (16,22–27). None of these studies, however, assess the initial outgrowth of individual sensory versus motor axons in CN V nor have individual axon trajectories been reconstructed from distinct sensory or motor neurons of origin toward distal or central targets. We recognized that to account for potentially subtle,

partially penetrant disruptions of initial differentiation of CN V sensory and motor neurons due to 22q11.2 gene deletion, it would be necessary to assess the growth of individual axons, to distinguish their sensory versus motor identities and to evaluate their trajectories and targeting in their native tissue volumes. Single growing axons have been visualized in whole invertebrates (28,29) and some vertebrates embryos (30–34) using selective molecular markers (34–36) to label individual axons in small, transparent embryos. Technical constraints of specificity and size, however, complicate similar analyses of axon growth in substantially larger mammalian embryos. Thus, we developed an *ex vivo* approach to label small subsets of individual CN V sensory or motor neuron and their axons in whole embryos. Our *ex vivo* biocytin tracing method does not require single cell injection, genetic recombination, viral infection, long survivals or histological processing. Our novel 3D confocal imaging approach along with advanced digital morphometric analysis allows us to unequivocally assess growth and targeting of individual CN sensory and motor neuron axons in native tissue volumes. This level of resolution was necessary to detect subtle, partially penetrant but quantitatively consistent phenotypes that result from early developmental consequences of diminished dosage of 22q11.2 genes in the hindbrain and craniofacial periphery.

## Patterning, signaling and cranial nerve development

Hindbrain A–P patterning establishes the identity of the central hindbrain motor neurons and peripheral neural crest-derived sensory neurons that comprise each nerve/ganglion, the location of each cranial nerve, and matches the projections of each cranial nerve to their targets (19,37–39). It has been difficult to disentangle the direct influence of A–P patterning on CN motor and sensory neuron differentiation versus additional modulation by extrinsic factors that further define neuronal identity as well as axon growth and guidance (40–44). Our results resolve some of this ambiguity in the context of 22q11.2 gene deletion. When hindbrain RA-dependent patterning and gene expression levels (6) are altered toward WT in $LgDel^{+/-}$:$Raldh2^{+/-}$ compound embryos, independent of restoring diminished 22q11.2 gene dosage (9), CN V gross differentiation as well as individual axon growth phenotypes return to WT. Apparently, RA signaling, in an A–P sensitive manner, modulates growth capacities of individual CN V sensory and motor axons downstream of 22q11.2 deletion. RA has long been implicated in motor (45,46) and sensory axon growth (47–50). Previous observations suggest that RA has both trophic (49) and axon trajectory/targeting influences (18,47,48) on cranial neurons. In these studies, however, it was difficult to distinguish specific RA effects versus broader morphogenetic consequences of mutations or experimental manipulations used. Here, we show that in response to local, altered RA-related hindbrain patterning, CN V motor and sensory neurons selectively modify their axon growth programs. Our data do not allow us to fully resolve whether these changes are exclusively due to the modulation of cranial motor and sensory neuron identity or altered interactions with hindbrain progenitors, neural crest or mesodermal cells the growing axons encounter in the Ba1A/B mesenchyme, which is also derived from anterior rhombomeres. Nevertheless, these RA-mediated changes establish a selective sensitivity of CN V sensory and motor neuron early axon outgrowth. The apparent consequences of RA-mediated dysregulation include the destabilization of branching and local growth that increase the probability of local defasciculation and misdirected growth in CN V due to 22q11.2 deletion.

## Destabilization of cranial sensory and motor axon growth

We found several cellular disruptions of the initial growth of single CN V sensory and motor axons. These changes are distinct from substantial anomalies of CN axon guidance associated with loss of function mutations of genes encoding adhesion molecules, tropic/trophic factors or transcription factors in which axon targeting is grossly incorrect, and axon growth or branching is dramatically disrupted (51–53). Diminished 22q11.2 gene dosage via a mechanism that includes but is not limited to *Ranbp1*-related disruption of RA-mediated A–P hindbrain patterning destabilizes the growth and guidance of individual axons locally and stochastically without compromising the initial establishment of basic segregation of CNgV sensory and motor neuron projections. These smaller discursions of individual axon growth, concatenated throughout the entire population in developing $LgDel^{+/-}$ mice or 22q11.2 deleted humans, could result in substantial variation in peripheral innervation and central connections within generally appropriate gross targets, leading to sub-optimal orofacial sensory-motor function. The disordered fasciculation and terminal branching in the mx and md branches of $LgDel^{+/-}$ as well as $Ranbp1^{-/-}$ CN V may be the result of anomalously branching or sprouting of a subset of early growing axons, identified here, whose aberrant trajectories subsequently misdirect additional later growing axons that would otherwise extend directly in coherent fascicles to their presumptive targets.

These phenotypes, like several others associated with heterozygous deletion of 22q11.2 genes (reviewed by 1,54), are subtle and variable. This partial penetrance may reflect stochastic variation in gene expression associated with aneuploidy (55,56), including in the $LgDel^{+/-}$ CNgV (7). Thus, at each critical step of CN V morphogenesis and differentiation: hindbrain and cranial placode patterning, neurogenesis or migration and early axon growth, 22q11.2 deletion in any individual embryo may yield variable cell-by-cell gene expression levels—ranging from 2 to 1 N to null—and similarly variable phenotypes. Some cells may retain transcriptional or differentiation states close to WT, while others have mild to extreme anomalies due to varying dosage or complete loss of function of one or several genes—either in the 22q11.2 region or beyond. CN V sensory and motor axon phenotypes in $LgDel^{+/-}$ and $Ranbp1^{-/-}$ embryos are similar, in register with disrupted RA-dependent hindbrain patterning and CN V gross dysmorphology. In $LgDel^{+/-}$ embryos, however, these phenotypes are less frequent and severe than in $Ranbp1^{-/-}$. In $LgDel^{+/-}$, 22q11.2 genes and additional genes that contribute to these phenotypes may have a range of expression levels from cell to cell in CN V sensory and motor neuron populations. In contrast, in $Ranbp1^{-/-}$ embryos, full loss of *Ranpb1* expression is shared by all relevant CN V-associated cells, perhaps leading to more consistent changes in gene expression and greater penetrance of CN V axon growth phenotypes. Further analysis of expression level variation in CN V sensory or motor neurons from $LgDel^{+/-}$, $Ranpb1^{+/-}$ and WT embryos would be necessary to assess a potential contribution of cell-by-cell stochastic gene expression to the individual axon phenotypes we have identified.

## Mid-gestation divergence and neo-natal dysfunction

The axon anomalies we report here may reflect the earliest divergence in developmental programs for CN V sensory and motor innervation that compromise orofacial sensory-motor

function at birth—most notably S/F/S. We showed previously that *LgDel*$^{+/-}$ pups have many features of dysphagia—S/F/S disruptions—seen in infants and toddlers with 22q11DS (5,6). The anatomical and behavioral changes are accompanied by additional changes in CNgV and craniofacial differentiation (3,57), as well as physiological and cellular changes in cranial motor neurons (58). We have identified an extremely early divergence in the developmental program that specifies optimal CN V differentiation. Concatenated changes that follow this disruption may diminish fidelity of motor and sensory innervation of oro-pharyngeal muscles or mechanoreceptive specializations engaged for optimal suckling, feeding and swallowing, or complicate subsequent activity and use-dependent refinement of connectivity (59,60). The precise relationship between the early divergence identified here, its relationship to initial disruption of hindbrain patterning, and the structural and functional integrity of trigeminal nerve innervation remain to be determined.

## Materials and Methods

### Animals

The George Washington University (GWU) Animal Research Facility maintained colonies of WT C57BL6/N (Charles River Laboratories), *LgDel*$^{+/-}$ (4), *Raldh2*$^{+/-}$ (61), *Tbx1*$^{+/-}$ (62) and *Ranbp1*$^{+/-}$ (13) mice. Timed pregnancies were generated using the date of vaginal plug as E0.5. All procedures were reviewed and approved by the GWU Institutional Animal Care Use Committee. After collection, prior to histological processing, all embryos were assessed for agreement between gestational ages and stages as described below.

### Biocytin injection and clearing

E11.5 embryos, in which Ba1A is the most prominent of the anterior branchial arches (see also Fig. 2), were harvested in PBS/0.5% heparin (H5515, Sigma, St. Louis, MO). These E11.5 embryos were then microinjected with 5% biocytin conjugated to Alexa Fluor 594, 488 (A12922 or A12924; ThermoFisher Sci., Waltham, MA) or 640 (92 007; Biotium, Fremont, CA) in 0.05 M $K_3PO_4$ buffer, pH 7.0 with 2% DMSO (63). About 20–40 nl biocytin was injected into target sites with a glass micropipette under microscopic observation using a pico-injector (PLI-100, Harvard Apparatus). Embryos were then rinsed in Leibovitz L-15 medium (SH30525.01; HyClone, San Angelo, TX; GE Healthcare Life Sci.), incubated in L-15/10% bovine calf serum (SH30073.02; HyClone) for 1.5 h in a 37°C humidified chamber, fixed with 4% paraformaldehyde [(PFA) in PBS, pH 7.4] and cleared using BABB: 1:2 Benzyl Alcohol (A395, Fisher Sci.)/Benzyl Benzoate (105 860 010, Fisher Sci.).

### Confocal microscopy and image analysis

Injected embryos were imaged with a Leica TCS SP8 multiphoton confocal microscope (Leica Microsystems, Buffalo Grove, IL), with a white laser source and Leica HyD-SMD Hybrid detector. Images were recorded with a DFC365FX camera at a resolution of 2048 × 2048 pixels using a 20× oil immersion objective (NA 0.75), a 1.2 times software zoom and a z-step size of 1.2 µm. Based on the excitation wavelength used, the optical resolution was 291 nm in the XY-plane and 1.6 µm in the Z-plane. Images were captured using the photon counting feature to detect both bright and dim signals and stitched to overcome the limited field of view of the high NA objective. Images were saved in the 'Lif' format and quantified on a Dell Intel Xeon E 5-2637V2 3.50 GHz PC workstation with a 12 GB NVIDIA TITAN Xp graphic card and 128 GB RAM using Imaris 9.2 (Bitplane, Zurich, Switzerland). To avoid image overlap, only sparsely labeled axons were selected for analysis. Axon tracing, 3D reconstruction and scoring were performed blind to genotype. 'Lif' files were flattened and converted to the 'Tif' format for illustration. Regions of interest were enlarged digitally for visual inspection and for 'higher magnification' panels in the figures.

### Immunolabeling and analysis

E10.5 embryos, in which Ba1A and Ba2 are of similar size and the olfactory pits are lateral and separate rather than medial and fused, were fixed, dehydrated and bleached to diminish background labeling as described previously (6) and then labeled with mouse monoclonal $\alpha$-$\beta$III tubulin antibody (Biolegend, San Diego, CA, 1:1000) for 3 days at 4°C. After extensive PBS/0.1% Tween washes, they were incubated overnight in 1:1000 goat $\alpha$-mouse IgG, Alexa Fluor 546 (ThermoFisher Sci.) or 1:500 goat $\alpha$-mouse IgG conjugated to HRP. After final PBS washes, fluorescent-labeled embryos were dehydrated, cleared in BABB and imaged confocally using 10× (NA 0.4) objective, a 1× software zoom and z-step size of 2.4 µm. Following DAB/$NiCl_2$ visualization of HRP, the additional embryos were dehydrated, cleared with BABB and imaged using a Leica Wild M420 photomacroscope. For sections, E11.5 Alexa Fluor 488-biocytin injected embryos were fixed, cryosectioned and then labeled with primary antibodies: mouse $\alpha$-Brn3A (Millipore, St. Louis, MO, 1:100), rabbit $\alpha$-Six1 (Proteintech, Rosemont, IL, 1:1500) or goat $\alpha$-Sox10 (Santa Cruz Biotechnology, Dallas, TX, 1:50) followed by detection with Alexa Fluor 546 secondary antibody.

### *In situ* hybridization

Digoxigenin-labeled *Cyp26b1* anti-sense and sense probes were synthesized using T3 and T7 RNA polymerase, respectively. *In situ* hybridization was performed on whole E9.5 embryos, selected for consistent developmental stage based upon branchial arch, otic vesicle and eye differentiation. The embryos were imaged and analyzed as previously described (6). Briefly, prior to imaging, some embryos were further dissected to isolate the hindbrain; the surface ectoderm overlying the nascent fourth ventricle was removed and preparations flattened slightly to better visualize the rhombencephalon.

### Quantitative and statistical analysis

Tortuosity was calculated as the ratio of axon length, measured digitally in 2D dimensional TIF images created from the image stacks based upon the distance between the axon origin at its parent cell body to its distal termination. Chi-square tests (Fisher Exact) compared frequencies of categorical variables (axon phenotypes: branching, misrouting and sprouting). Single continuous variables (tortuosity) were compared using *t*-tests. Multiple continuous variables (phenotypes/axons) were analyzed by one-way ANOVA with Bonferroni correction using Prism 6 (GraphPad, San Diego, CA). Statistical significance was accepted at $P \leq 0.05$. Gross CN V phenotypes in whole mount embryos labeled for $\beta$III tubulin (*Ranbp1*$^{-/-}$, *Ranbp1*$^{+/-}$ and WT) were compared using the Fisher Exact test. For all analyses, WT littermates were collected along with mutant embryos in the same litter (Table 1). The WT control sample ($n = 56$ axons/13 embryos/9 litters) for individual axon phenotypes was a composite of single axons labeled in WT littermates collected across litters with all mutant genotypes.

## Acknowledgements

We are grateful to Michael Fox for helpful comments on the manuscript.

*Conflict of Interest statement*. None declared.

## Funding

National Institute of Child Health and Human Development (P01 HD083157 to A.S.L.); NICHD IDDRC U54 (HD 090257 to G.W.); Georgetown University and Children's National Medical Center.

## References

1. Meechan, D.W., Maynard, T.M., Tucker, E.S., Fernandez, A., Karpinski, B.A., Rothblat, L.A. and LaMantia, A.S. (2015) Modeling a model: mouse genetics, 22q11.2 deletion syndrome, and disorders of cortical circuit development. *Prog. Neurobiol.*, **130**, 1–28.
2. Del Pino, I., Rico, B. and Marin, O. (2018) Neural circuit dysfunction in mouse models of neurodevelopmental disorders. *Curr. Opin. Neurobiol.*, **48**, 174–182.
3. Maynard, T.M., Zohn, I.E., Moody, S.A. and LaMantia, A.S. (2020) Suckling, feeding, and swallowing: behaviors, circuits, and targets for neurodevelopmental pathology. *Annu. Rev. Neurosci.*, **43**, 315–336.
4. Merscher, S., Funke, B., Epstein, J.A., Heyer, J., Puech, A., Lu, M.M., Xavier, R.J., Demay, M.B., Russell, R.G., Factor, S. *et al.* (2001) Tbx1 is responsible for cardiovascular defects in velo-cardio-facial/Digeorge syndrome. *Cell*, **104**, 619–629.
5. LaMantia, A.S., Moody, S.A., Maynard, T.M., Karpinski, B.A., Zohn, I.E., Mendelowitz, D., Lee, N.H. and Popratiloff, A. (2016) Hard to swallow: developmental biological insights into pediatric dysphagia. *Dev. Biol.*, **409**, 329–342.
6. Karpinski, B.A., Maynard, T.M., Fralish, M.S., Nuwayhid, S., Zohn, I.E., Moody, S.A. and LaMantia, A.S. (2014) Dysphagia and disrupted cranial nerve development in a mouse model of Digeorge (22q11) deletion syndrome. *Dis. Model. Mech.*, **7**, 245–257.
7. Maynard, T.M., Horvath, A., Bernot, J.P., Karpinski, B.A., Tavares, A.L.P., Shah, A., Zheng, Q., Spurr, L., Olender, J., Moody, S.A. *et al.* (2020) Transcriptional dysregulation in developing trigeminal sensory neurons in the Lgdel mouse model of Digeorge 22q11.2 deletion syndrome. *Hum. Mol. Genet.*, **29**, 1002–1017.
8. Yitsege, G., Stokes, B.A., Sabatino, J.A., Sugrue, K.F., Banyai, G., Paronett, E.M., Karpinski, B.A., Maynard, T.M., LaMantia, A.S. and Zohn, I.E. (2020) Variations in maternal vitamin a intake modifies phenotypes in a mouse model of 22q11.2 deletion syndrome. *Birth Defects Res.*, in press.
9. Maynard, T.M., Gopalakrishna, D., Meechan, D.W., Paronett, E.M., Newbern, J.M. and LaMantia, A.S. (2013) 22q11 gene dosage establishes an adaptive range for sonic hedgehog and retinoic acid Signaling during early development. *Hum. Mol. Genet.*, **22**, 300–312.
10. Vitelli, F., Morishima, M., Taddei, I., Lindsay, E.A. and Baldini, A. (2002) Tbx1 mutation causes multiple cardiovascular defects and disrupts neural crest and cranial nerve migratory pathways. *Hum. Mol. Genet.*, **11**, 915–922.
11. Calmont, A., Ivins, S., Van Bueren, K.L., Papangeli, I., Kyriakopoulou, V., Andrews, W.D., Martin, J.F., Moon, A.M., Illingworth, E.A., Basson, M.A. *et al.* (2009) Tbx1 controls cardiac neural crest cell migration during arch artery development by regulating Gbx2 expression in the pharyngeal ectoderm. *Development*, **136**, 3173–3183.
12. Calmont, A., Anderson, N., Suntharalingham, J.P., Ang, R., Tinker, A. and Scambler, P.J. (2018) Defective vagal innervation in murine Tbx1 mutant hearts. *J. Cardiovasc. Dev. Dis.*, **5**.
13. Paronett, E.M., Meechan, D.W., Karpinski, B.A., LaMantia, A.S. and Maynard, T.M. (2015) Ranbp1, deleted in Digeorge/22q11.2 deletion syndrome, is a microcephaly gene that selectively disrupts layer 2/3 cortical projection neuron generation. *Cereb. Cortex*, **25**, 3977–3993.
14. Niederreither, K., Vermot, J., Schuhbaur, B., Chambon, P. and Dolle, P. (2000) Retinoic acid synthesis and hindbrain patterning in the mouse embryo. *Development*, **127**, 75–85.
15. Maynard, T.M., Haskell, G.T., Bhasin, N., Lee, J.M., Gassman, A.A., Lieberman, J.A. and LaMantia, A.S. (2002) Ranbp1, a Velocardiofacial/Digeorge syndrome candidate gene, is expressed at sites of mesenchymal/epithelial induction. *Mech. Dev.*, **111**, 177–180.
16. Erzurumlu, R.S., Murakami, Y. and Rijli, F.M. (2010) Mapping the face in the somatosensory brainstem. *Nat. Rev. Neurosci.*, **11**, 252–263.
17. Davies, A.M. and Lumsden, A.G. (1986) Fasciculation in the early mouse trigeminal nerve is not ordered in relation to the emerging pattern of whisker follicles. *J. Comp. Neurol.*, **253**, 13–24.
18. Karpinski, B.A., Bryan, C.A., Paronett, E.M., Baker, J.L., Fernandez, A., Horvath, A., Maynard, T.M., Moody, S.A. and LaMantia, A.S. (2016) A cellular and molecular mosaic establishes growth and differentiation states for cranial sensory neurons. *Dev. Biol.*, **415**, 228–241.
19. Guthrie, S. (2007) Patterning and axon guidance of cranial motor neurons. *Nat. Rev. Neurosci.*, **8**, 859–871.
20. Brugmann, S.A., Pandur, P.D., Kenyon, K.L., Pignoni, F. and Moody, S.A. (2004) Six1 promotes a placodal fate within the lateral neurogenic ectoderm by functioning as both a transcriptional activator and repressor. *Development*, **131**, 5871–5881.
21. Schlosser, G. and Ahrens, K. (2004) Molecular anatomy of placode development in *Xenopus laevis*. *Dev. Biol.*, **271**, 439–466.
22. Erzurumlu, R.S., Chen, Z.F. and Jacquin, M.F. (2006) Molecular determinants of the face map development in the trigeminal brainstem. *Anat. Rec. A Discov. Mol. Cell Evol. Biol.*, **288**, 121–134.
23. Ulupinar, E., Jacquin, M.F. and Erzurumlu, R.S. (2000) Differential effects of Ngf and Nt-3 on embryonic trigeminal axon growth patterns. *J. Comp. Neurol.*, **425**, 202–218.
24. Bouheraoua, N., Fouquet, S., Marcos-Almaraz, M.T., Karagogeos, D., Laroche, L. and Chedotal, A. (2019) Genetic analysis of the organization, development, and plasticity of corneal innervation in mice. *J. Neurosci.*, **39**, 1150–1168.
25. McKenna, C.C. and Lwigale, P.Y. (2011) Innervation of the mouse cornea during development. *Invest. Ophthalmol. Vis. Sci.*, **52**, 30–35.
26. Kubilus, J.K. and Linsenmayer, T.F. (2010) Developmental guidance of embryonic corneal innervation: roles of Semaphorin3a and Slit2. *Dev. Biol.*, **344**, 172–184.
27. Laumonnerie, C., Bechara, A., Vilain, N., Kurihara, Y., Kurihara, H. and Rijli, F.M. (2015) Facial whisker pattern is not sufficient to instruct a whisker-related topographic map in the mouse somatosensory brainstem. *Development*, **142**, 3704–3712.
28. Ehrhardt, E., Kleele, T. and Boyan, G. (2015) A method for Immunolabeling neurons in intact cuticularized insect appendages. *Dev. Genes Evol.*, **225**, 187–194.
29. Zito, K., Parnas, D., Fetter, R.D., Isacoff, E.Y. and Goodman, C.S. (1999) Watching a synapse grow: noninvasive

confocal imaging of synaptic growth in drosophila. *Neuron*, **22**, 719–729.
30. Diekmann, H., Kalbhen, P. and Fischer, D. (2015) Characterization of optic nerve regeneration using transgenic zebrafish. *Front. Cell. Neurosci.*, **9**, 118.
31. St John, J.A. and Key, B. (2012) Huc-Egfp mosaic labelling of neurons in zebrafish enables in vivo live cell imaging of growth cones. *J. Mol. Histol.*, **43**, 615–623.
32. Andersen, E.F., Asuri, N.S. and Halloran, M.C. (2011) In vivo imaging of cell behaviors and F-actin reveals Lim-Hd transcription factor regulation of peripheral versus central sensory axon development. *Neural Dev.*, **6**, 27.
33. Palanca, A.M., Lee, S.L., Yee, L.E., Joe-Wong, C., Trinh le, A., Hiroyasu, E., Husain, M., Fraser, S.E., Pellegrini, M. and Sagasti, A. (2013) New transgenic reporters identify somatosensory neuron subtypes in larval zebrafish. *Dev. Neurobiol.*, **73**, 152–167.
34. Pan, Y.A., Freundlich, T., Weissman, T.A., Schoppik, D., Wang, X.C., Zimmerman, S., Ciruna, B., Sanes, J.R., Lichtman, J.W. and Schier, A.F. (2013) Zebrabow: multispectral cell labeling for cell tracing and lineage analysis in zebrafish. *Development*, **140**, 2835–2846.
35. Chen, Y., Akin, O., Nern, A., Tsui, C.Y., Pecot, M.Y. and Zipursky, S.L. (2014) Cell-type-specific labeling of synapses in vivo through synaptic tagging with recombination. *Neuron*, **81**, 280–293.
36. Nicolai, L.J., Ramaekers, A., Raemaekers, T., Drozdzecki, A., Mauss, A.S., Yan, J., Landgraf, M., Annaert, W. and Hassan, B.A. (2010) Genetically encoded dendritic marker sheds light on neuronal connectivity in drosophila. *Proc. Natl. Acad. Sci. USA.*, **107**, 20553–20558.
37. Gaufo, G.O., Wu, S. and Capecchi, M.R. (2004) Contribution of Hox genes to the diversity of the hindbrain sensory system. *Development*, **131**, 1259–1266.
38. Parker, H.J., Pushel, I. and Krumlauf, R. (2018) Coupling the roles of Hox genes to regulatory networks patterning cranial neural crest. *Dev. Biol.*, **444**(Suppl 1), S67–S78.
39. Trainor, P.A. and Krumlauf, R. (2000) Patterning the cranial neural crest: hindbrain segmentation and Hox gene plasticity. *Nat. Rev. Neurosci.*, **1**, 116–124.
40. Panagiotaki, N., Dajas-Bailador, F., Amaya, E., Papalopulu, N. and Dorey, K. (2010) Characterisation of a new regulator of Bdnf signalling, Sprouty3, involved in axonal morphogenesis in vivo. *Development*, **137**, 4005–4015.
41. Fujita, N. and Nagata, S. (2007) Contactin 1 knockdown in the hindbrain induces abnormal development of the trigeminal sensory nerve in Xenopus embryos. *Dev. Genes Evol.*, **217**, 709–713.
42. Haremaki, T., Deglincerti, A. and Brivanlou, A.H. (2015) Huntingtin is required for ciliogenesis and neurogenesis during early Xenopus development. *Dev. Biol.*, **408**, 305–315.
43. Engelhard, C., Sarsfield, S., Merte, J., Wang, Q., Li, P., Beppu, H., Kolodkin, A.L., Sucov, H.M. and Ginty, D.D. (2013) Megf8 is a modifier of Bmp signaling in trigeminal sensory neurons. *Elife*, **2**, e01160.
44. Simon, E., Theze, N., Fedou, S., Thiebaud, P. and Faucheux, C. (2017) Vestigial-like 3 is a novel Ets1 interacting partner and regulates trigeminal nerve formation and cranial neural crest migration. *Biol. Open*, **6**, 1528–1540.
45. Maden, M. (2007) Retinoic acid in the development, regeneration and maintenance of the nervous system. *Nat. Rev. Neurosci.*, **8**, 755–765.
46. Maden, M., Ong, D.E. and Chytil, F. (1990) Retinoid-binding protein distribution in the developing mammalian nervous system. *Development*, **109**, 75–80.
47. LaMantia, A.S., Bhasin, N., Rhodes, K. and Heemskerk, J. (2000) Mesenchymal/epithelial induction mediates olfactory pathway formation. *Neuron*, **28**, 411–425.
48. Hornberg, M., Gussing, F., Berghard, A. and Bohm, S. (2009) Retinoic acid selectively inhibits death of basal vomeronasal neurons during late stage of neural circuit formation. *J. Neurochem.*, **110**, 1263–1275.
49. Whitesides, J., Hall, M., Anchan, R. and LaMantia, A.S. (1998) Retinoid signaling distinguishes a subpopulation of olfactory receptor neurons in the developing and adult mouse. *J. Comp. Neurol.*, **394**, 445–461.
50. Wang, G. and Scott, S.A. (2008) Retinoid signaling is involved in governing the waiting period for axons in Chick Hindlimb. *Dev. Biol.*, **321**, 216–226.
51. Aberle, H. (2019) Axon guidance and collective cell migration by substrate-derived attractants. *Front. Mol. Neurosci.*, **12**, 148.
52. Gofflot, F. and Lizen, B. (2018) Emerging roles for Hox proteins in synaptogenesis. *Int. J. Dev. Biol.*, **62**, 807–818.
53. Stoeckli, E.T. (2018) Understanding axon guidance: are we nearly there yet? *Development*, **145**.
54. Motahari, Z., Moody, S.A., Maynard, T.M. and LaMantia, A.S. (2019) In the line-up: deleted genes associated with Digeorge/22q11.2 deletion syndrome: are they all suspects? *J. Neurodev. Disord.*, **11**, 7.
55. Stamoulis, G., Garieri, M., Makrythanasis, P., Letourneau, A., Guipponi, M., Panousis, N., Sloan-Bena, F., Falconnet, E., Ribaux, P., Borel, C. *et al.* (2019) Single cell transcriptome in aneuploidies reveals mechanisms of gene dosage imbalance. *Nat. Commun.*, **10**, 4495.
56. Herve, B., Coussement, A., Gilbert, T., Dumont, F., Jacques, S., Cuisset, L., Chicard, M., Hizem, S., Bourdoncle, P., Letourneur, F. *et al.* (2016) Aneuploidy: the impact of chromosome imbalance on nuclear organization and overall genome expression. *Clin. Genet.*, **90**, 35–48.
57. Welby, L., Caudill, H., Yitsege, G., Hamad, A., Bunyak, F., Zohn, I.E., Maynard, T., LaMantia, A.S., Mendelowitz, D. and Lever, T.E. (2020) Persistent feeding and swallowing deficits in a mouse model of 22q11.2 deletion syndrome. *Front. Neurol.*, **11**, 4.
58. Wang, X., Bryan, C., LaMantia, A.S. and Mendelowitz, D. (2017) Altered neurobiological function of brainstem hypoglossal neurons in Digeorge/22q11.2 deletion syndrome. *Neuroscience*, **359**, 1–7.
59. Jenkins, B.A. and Lumpkin, E.A. (2017) Developing a sense of touch. *Development*, **144**, 4078–4090.
60. Widmer, C.G. and Morris-Wiman, J. (2010) Limb, respiratory, and masticatory muscle compartmentalization: developmental and hormonal considerations. *Prog. Brain Res.*, **187**, 63–80.
61. Mic, F.A., Haselbeck, R.J., Cuenca, A.E. and Duester, G. (2002) Novel retinoic acid generating activities in the neural tube and heart identified by conditional rescue of Raldh2 null mutant mice. *Development*, **129**, 2271–2282.
62. Jerome, L.A. and Papaioannou, V.E. (2001) Digeorge syndrome phenotype in mice mutant for the T-Box gene, Tbx1. *Nat. Genet.*, **27**, 286–291.
63. Popratiloff, A. and Peusner, K.D. (2007) Otolith fibers and terminals in chick vestibular nuclei. *J. Comp. Neurol.*, **502**, 19–37.